www.elsevier.com/locate/pss

The OH Venus nightglow spectrum: intensity and vibrational composition from VIRTIS-Venus Express observations

Lauriane Soret, Jean-Claude Gérard, Giuseppe Piccioni, Pierre Drossart

PII: S0032-0633(12)00234-6
DOI: http://dx.doi.org/10.1016/j.pss.2012.07.027
Reference: PSS3372

To appear in: *Planetary and Space Science*

Received date: 28 February 2012
Revised date: 13 June 2012
Accepted date: 20 July 2012

Cite this article as: Lauriane Soret, Jean-Claude Gérard, Giuseppe Piccioni and Pierre Drossart, The OH Venus nightglow spectrum: intensity and vibrational composition from VIRTIS-Venus Express observations, *Planetary and Space Science,* http://dx.doi.org/10.1016/j.pss.2012.07.027

The OH Venus nightglow spectrum: intensity and vibrational composition from VIRTIS-Venus Express observations

Lauriane Soret[1], Jean-Claude Gérard[1]

JC.Gerard@ulg.ac.be

[2]INAF-IAPS, Rome, Italy

Giuseppe Piccioni[2]

Giuseppe.Piccioni@iaps.inaf.it

Pierre Drossart[3]

Pierre.Drossart@obspm.fr

[1]Laboratoire de Physique Atmosphérique et Planétaire, Université de Liège, Liège, Belgium

[3]Observatoire de Paris - Meudon, LESIA, Meudon, France

Submitted for publication to Planetary and Space Science June 2012

Abstract

Limb spectra of the OH nightglow emission corresponding to the Δv=1 and Δv=2 sequences have been collected with the VIRTIS infrared imaging spectrograph on board Venus Express between April 2006 and October 2008. A detailed statistical analysis shows that the peak intensity and altitude of the two vibrational sequences are significantly correlated, with a mean intensity ratio of the two sequences of 0.38±0.37. The altitude of the maximum of the Δv=2 emission is located ~1 km lower than Δv=1. A spectral analysis shows that the Δv=1 sequence is composed at 44.6% by the (1-0) band, 9.3% by the (3-2) band and 7.1% by the (4-3) band. The Δv=2 emission is best fitted if solely including the (2-0) band.

A non-LTE model of OH vibrational population by the O_3 + H reaction including radiative and collisional relaxation has been used to compare the expected spectral distribution, the altitude of the emission peak and the emission rate under different assumptions on the quenching processes to those observed with VIRTIS. The adopted carbon dioxide, atomic

oxygen and ozone densities are based on recent Venus Express remote sensing measurements. We find that the "sudden death" quenching scheme by CO_2 produces inadequate spectral distribution between the various bands and insufficient airglow brightness. Instead, the observed spectral distribution and the total emission intensity are reasonably well reproduced with the single quantum jump model, a O density profile peaking at 103.5 km with a maximum value of 1.9×10^{11} cm^{-3}, a O_3 density profile peaking at 5.8×10^6 cm^{-3} at 96.5 km and a H density profile close to 10^8 cm^{-3} between 90 and 120 km, in agreement with several photochemical models.

- The infrared OH Meinel bands have been observed by VIRTIS on board Venus Express.
- The Δv=1 and Δv=2 sequences are significantly correlated in altitude and intensity.
- Most of the population is in the lower vibrational levels.
- A non-LTE model was developed using O, O_3 and CO_2 densities from VEX measurements.
- Observations are reproduced with these densities and a single quantum jump model.

1. Introduction

The OH Venus nightglow infrared emission of the Meinel bands, populated by low vibrational levels, was recently observed by *Piccioni et al.* (2008). Even more recently, *Montmessin et al.* (2011) discovered the presence of O_3 in the nightside upper atmosphere. This detection seems to confirm the *Bates and Nicolet* (1950) mechanism to explain the production of excited OH molecules in both the visible and infrared domains:

$$H + O_3 \rightarrow OH\left(X\,^2\Pi, v \leq 9\right) + O_2 \qquad (1)$$

This mechanism was proposed after *Meinel* (1950) discovered the existence of high vibrational levels of the OH visible and near infrared airglow in the terrestrial mesosphere. Another possible source of vibrationally excited hydroxyl is the process:

$$O + HO_2 \rightarrow OH\left(X\,^2\Pi\right) + O_2 \quad (2)$$

In his review of the terrestrial OH airglow, *Meriwether* (1989) concluded that, on Earth, reaction (2) is a negligible source of excited OH compared to the Bates-Nicolet mechanism (1). The same conclusion was reached by *Krasnopolsky* (2011) for the Venus nightside mesosphere. While the OH emission has never been detected on Mars, the OH nightglow was discovered in the Venus nightside atmosphere by *Piccioni et al.* (2008). They clearly identified the (1-0) and (2-1) transitions at 2.80 and 2.94 μm, respectively, and the (2-0) transition at 1.43 μm in a limb spectrum acquired with the Visible and Infra-Red Thermal Imaging Spectrometer (VIRTIS) instrument on board the Venus Express spacecraft. The retrieved (1-0) transition limb intensity was 0.88 ± 0.09 MR (1 Rayleigh, R, corresponds to the brightness of an extended source emitting 10^6 photons cm^{-2} s^{-1} in 4π sr) while the (2-0) intensity was 0.10 ± 0.04 MR. They both peaked at 96 ± 2 km. Using 334 limb profiles from the VIRTIS instrument, *Gérard et al.* (2010) measured an average peak intensity of 0.41 ± 0.37 MR for the Δv=1 sequence and a mean peak altitude of 95.3 ± 3 km. Finally, the full set of VIRTIS-M limb observations of the OH Venus nightglow was analyzed by *Soret et al.* (2010). Based on 3328 limb profiles, they found that the mean peak intensity along the line of sight of the Δv = 1 sequence is $0.35^{+0.35}_{-0.21}$ MR and is localized at 96.4 ± 5 km. The error bar of ± 5 km corresponds to the width at half maximum of the distribution of the minimum ray height at the emission peak. Using a ground-based telescope and long exposure times, *Krasnopolsky* (2010) obtained infrared high-resolution spectra of the (1-0) P1(4.5) and (2-1) Q1(1.5) OH airglow lines. The corresponding total OH intensity was in good agreement with the VIRTIS observations. A more detailed description of the OH emission observations in the terrestrial and Venusian atmospheres was given by *Migliorini et al.* (2010).

The recent detection of ozone near 100 km by the Spectroscopy for Investigation of Characteristics of the Atmosphere of Venus (SPICAV) instrument on board Venus Express by

Montmessin et al. (2011) provides support for the Bates–Nicolet mechanism as the main chemical reaction to produce excited OH in the Venus atmosphere. Nevertheless, this mechanism initially mainly populates the v=6-9 vibrational levels. By contrast, section 2 will show that only low vibrational levels of the OH emission are observed in Venus spectra. Several models will be presented in section 3 to explain this apparent inconsistency.

2. Limb observations of the OH (Δv=1) and (Δv=2) nightglows

1.1. VIRTIS observations

The VIRTIS instrument is an imaging spectrometer on board the Venus Express satellite. The spacecraft started orbiting Venus in April 2006 on an elliptical orbit with a period of 24h, a low-altitude pericenter located at high northern latitudes and an apocenter of 66,000 km. VIRTIS-M-IR covers the infrared spectral range from 1 to 5 μm and can observe both in nadir and limb viewing geometries (*Drossart et al.*, 2007; *Piccioni et al.*, 2009). Observations with VIRTIS-M were made between 14 April 2006 (orbit VI0023_01) and 14 October 2008 (orbit VI0907_05). Since the infrared OH emission is very weak compared to the thermal emission of the planet, it is impossible to detect the OH emission in the nadir geometry. Instead, the OH emission is more easily observed at the limb since intensities are integrated along the line of sight and are thus amplified by a factor close to 50. Despite this limb brightening, the less intense Δv=2 sequence is generally difficult to detect. The entire VIRTIS-M-IR dataset has been considered for this study and a total of 4501 limb images were collected. However, the eccentricity of the elliptical orbit is such that the spacecraft-distance is so long in the southern hemisphere that corresponding limb profiles are significantly smoothed by the instrumental

field of view. The resolution at the apocenter (situated 66,000 km away from the planet) is 15 km while it is 1.8 km near the equator. Thus, the limb profiles used in this study were mainly obtained in the northern hemisphere of the planet. Two important quantities can be obtained from these observations: the spectral distribution and the intensity profiles of both the Δv=1 and Δv=2 emissions.

1.2. Spectral analysis

Observations made with VIRTIS-M-IR consist of an image cube for each spectral channel, from 1 to 5 μm, by steps of 9.5 nm. It is thus possible to obtain complete spectra, where the Δv=1 and Δv=2 Meinel bands can be identified between 2.7 and 3.1 μm and near 1.43 μm, respectively (see Figure 1 in *Piccioni et al.* (2008) and Figure 1 in *Gérard et al.* (2010)). In order to improve the signal to noise ratio, we have generated an average spectrum based on the eight orbits showing the brightest OH emissions. For each orbit, a mean spectrum was calculated by taking into account the intensity of all pixels located within 2 km from the peak of the associated limb profile. Figures 1a and 1b represent these average normalized spectra for the Δv=1 and Δv=2 sequences (in black).

In order to analyze the intensity distribution of both the Δv=1 and Δv=2 sequences, synthetic spectra were generated with the PGOPHER (a Program for Simulating Rotational Structure, C. M. Western, University of Bristol, http://pgopher.chm.bris.ac.uk) software at the temperature of the OH airglow layer. This temperature can easily be determined as: (i) the OH and the $O_2(a^1\Delta)$ airglow layers are both located at ~96 km (*Gérard et al.*, 2010; *Migliorini et al.*, 2010; *Soret et al.*, 2010), and (ii) the temperature of the Venus nightside at 96 km has been derived from the intensity distribution of the rotational lines in the $O_2(a^1\Delta)$ airglow band at 1.27 μm in several studies and found to be ~185±15 K (Table 3 from *Bailey et al.*, 2008;

Ohtsuki et al., 2008; *Krasnopolsky*, 2010). The relative intensities of the lines within the (1-0), (2-1), (3-2), (4-3), (2-0) and (3-1) OH Meinel bands have been computed at 185 K. The line intensities were generated using the appropriate Boltzmann factor and partition function for the rotational levels of the $X\,^2\Pi$ state. The transition constants taking into account the rotation, the spin-rotation, the lambda-doubling and the spin-orbit interactions were taken from *Bernath and Colin* (2009). These synthetic spectra for each of the six bands were subsequently convolved by the VIRTIS point spread function, which is well represented by a Gaussian function with a full width at half maximum of 18 nm. The structure of these bands is shown in Figure 1a and Figure 1b. By assembling them together and adjusting their relative weight to match the observed spectrum, a global synthetic spectrum was obtained (in red in Figure 1a and Figure 1b). This best fit corresponds to the following contributions to the Δv=1 sequence: 44.6% in the (1-0) band, 39.0% in the (2-1) band, 9.3% in the (3-2) band and 7.1% in the (4-3) band, while the Δv=2 emission is best fitted if solely including the (2-0) band (Figure 1b). In order to study the impact of the temperature variations due to the changing nature of the downwelling portion of the subsolar-to-antisolar circulation in this region of the atmosphere, the same calculation was repeated at 170 K and 200 K. The results vary by less than 1.5 %. It is important to stress that only low vibrational levels contribute to the observed Δv=1 and Δv=2 sequences.

1.3. Limb intensity profiles analysis

Intensity profiles can also be deduced from limb observations. They represent the OH emission as a function of the altitude of the minimum ray height of the line of sight through the atmosphere. The procedure applied to extract limb profiles from VIRTIS images was described in detail by *Gérard et al.* (2010) and *Soret et al.* (2010). All pixels from 2.7 to 3.1

μm for the Δv=1 emission and 1.4 to 1.5 μm for Δv=2 with identical latitude, local time and altitude have been averaged. No correction for the field of view of the instrument has been applied since the data were collected in the northern hemisphere, where the spacecraft gets closer to the planet. Near the equator, the resolution of VIRTIS at the limb is 1.8 km and it improves as the spacecraft moves toward higher northern latitudes. Examples of such limb profiles were illustrated in Figure 1 by *Migliorini et al.* (2010) and in Figure 1 by *Soret et al.* (2010). For a given orbit, *Migliorini et al.* (2010) showed that the limb intensity of the (2-0) transition is significantly weaker than the (1-0) emission. *Soret et al.* (2010) showed that an underlying contribution probably caused by scattering of thermal emission by high altitude haze must be removed from the Δv=1 limb profiles. In the present study, a total of 650 profiles showing a measureable emission peak for both the Δv=1 and the Δv=2 sequences have been processed in the same way. The next paragraph presents the results of the statistical study based on this database.

This statistical study is based on the values of the peak altitude and the peak intensity of the previous 650 simultaneous Δv=1 and Δv=2 limb profiles. Figure 2a is a histogram representing the distribution of the altitude of the Δv=1 (in red) and the Δv=2 (in black) maximum emission along the line of sight. The shapes of both distributions are very similar, the red histogram being slightly shifted toward the right. This suggests that the Δv=1 emission globally occurs at a slightly higher altitude than the Δv=2 emission. The mode of both distributions is located at 97 km and the mean values are 96.5±3.6 and 95.7±3.3 km, respectively. To test whether this difference of altitude is significant, the Wilcoxon matched-pairs signed-ranks non-parametric statistical test was performed. We calculate the quantity:

$$Z = \frac{T - \frac{n(n+1)}{4}}{\sqrt{\frac{n(n+1)(2n+2)}{24}}} \quad (3)$$

where n=650 is the number of simultaneous observations, $T = \left| \sum_{i=1}^{n} \mathrm{sgn}\left(alt_{2,i} - alt_{1,i}\right) \times R_i \right|$, R_i is the rank of the i-th observation and $alt_{1,i}$ and $alt_{2,i}$ represent the peak altitudes of all paired observations of the Δv=1 and the Δv=2, respectively. Comparing the Z value to the significance tables, the p-value for the null hypothesis is found to be <0.000001, which means that the median of the altitude differences is not equal to zero. The difference of altitudes being statistically highly significant, we can conclude that the Δv=1 emission layer is located ~0.8 km above that of Δv=2. Figure 1 in *Migliorini et al.* (2010) perfectly illustrates this situation.

Figure 2b is a histogram representing the distribution of the peak intensity of the Δv=1 (in red) and the Δv=2 (in black) intensity along the line of sight. Both distributions present a peak at low intensities and a tail towards higher values. The Δv=1 emission is about three times brighter than Δv=2. The averaged slant intensities at the peak are I_1=0.60±0.44 and I_2=0.23±0.15 MR, respectively. The observed mean ratio I_2/I_1 is thus equal to 0.38±0.37. The scatter is quite important but this ratio is important as will be discussed in the modelling section. The I_1 value of 0.60 MR is greater than that of 0.35 MR from *Soret et al.* (2010) since only the brightest spectra have been considered in this study so the Δv=2 sequence could also be simultaneously observed. If we assume that the OH(Δv=2) had been detected in every observation, the corresponding intensity would have been $I_2 = I_1 \times \frac{I_2}{I_1} = 0.35 \times 0.38 = 0.13$ MR. The intensity correlation of both sequences is described hereafter.

Figure 2c represents the altitude of the Δv=2 peak altitude as a function of the Δv=1 peak altitude. The linear regression shows that both emissions tend to increase in parallel. The linear correlation coefficient was found equal to R=0.39. To assess the significance of this parameter, the null hypothesis was tested by comparing the R value to the standard deviation $s_0 = \sqrt{n-1}$. The level of confidence that R is significantly different from zero is found to exceed 99.99%, implying that, despite a low correlation coefficient, the peak altitude of the Δv=1 and Δv=2 emissions cannot be considered as uncorrelated.

Finally, Figure 2d illustrates the fact that the Δv=2 peak intensity increases with the Δv=1 peak brightness. Despite some outlying points on the top left region of the plot, the correlation is clearly observed. The level of confidence that the correlation coefficient R=0.58 is significantly different from zero exceeds 99.99%. The outliers have visually been inspected to check that the spectra confirm the presence of both the Δv=1 and Δv=2 sequences and verify that the associated limb profiles show a regular shape. This inspection confirms that, in a limited number of cases, the Δv=2 emission can be as bright as (or even brighter than) the Δv=1 emission.

To summarize this statistical study, we have shown that the intensity along the line of sight of both emissions are correlated, they both peak near 97 km, even though the Δv=1 emission layer occurs at a slightly higher altitude than Δv=2, and that I_2/I_1=0.38±0.37. Previous studies (*Gérard et al.*, 2010; *Soret et al.*, 2010) also demonstrated that the peak altitude and the peak brightness of the Δv=1 emission are uncorrelated: the peak intensity decreases while moving from the antisolar point to the terminator, while the peak altitude remains constant.

3. Modeling the Δv=1 and Δv=2 emissions

As mentioned in section 1, the Bates-Nicolet mechanism (reaction 1) produces excited OH in vibrational levels up to v=9. However, the spectral study presented in section 2.1 concludes that only transitions from upper vibrational levels less than v'=4 are detected in VIRTIS resolution spectra of the Venus mesosphere. Various models have been considered in the present section in order to explain this behavior. These models take into account the production of excited OH (reaction 1) but also its deactivation by collisional quenching (reactions 4 and 6), reactive loss (reaction 5) and spontaneous emission (reaction 7):

$$OH\left(v'\right)+O \rightarrow OH\left(v''=0\right)+O \quad (4)$$

$$OH\left(v'\right)+O \rightarrow O_2+H \quad (5)$$

$$OH\left(v'\right)+CO_2 \rightarrow OH\left(v''\right)+CO_2 \quad (6)$$

$$OH\left(v'\right) \rightarrow OH\left(v''\right)+h\upsilon \quad (7)$$

Additional processes related to the chemical kinetics that determines the atmospheric composition do not have to be considered as they proceed at a much slower rate than vibrational deactivation. For instance, reaction (2) can be considered as negligible compared to reaction (1) as the $H+O_3$ reaction rate exceeds that of $O+HO_2$ by an order of magnitude (*Krasnopolsky*, 2011). Assuming steady state, the non-LTE OH density of each vibrational level can thus be calculated using the formula proposed by *García Muñoz et al.* (2005):

$$\left[OH\left(v\right)\right]=\frac{f\left(v\right)k_1\left[H\right]\left[O_3\right]+\sum_{9\geq v^*>v}\left(A\left(v^*,v\right)+k^{CO_2}\left(v^*,v\right)\left[CO_2\right]\right)\times\left[OH\left(v^*\right)\right]}{A_T\left(v\right)+k_T^{CO_2}\left(v\right)\left[CO_2\right]+\left(k^O\left(v\right)+K^O\right)\left[O\right]}$$

(8)

where k_1 is the rate coefficient (*Sander et al.*, 2003) and *f(v)* is the nascent fractional yield of level *v* in reaction 1. The *f(v)* values have been taken from *Ohoyama et al.* (1985) as adjusted by *García Muñoz et al.* (2005) (Table 1). The second term of equation (8) corresponds to indirect sources of OH(v) by spontaneous emissions and collisional quenching from higher vibrational levels. The *A* coefficients are the transition probabilities of spontaneous emission (process 7). They are taken from *Murphy* (1971) and have been adjusted by *García Muñoz et al.* (2005) to fit the absolute transition probability $A_T\left(v'\right)=\sum_{v''}A\left(v',v''\right)$ calculated by *Turnbull and Lowe* (1989). In formula (8), [*H*], [O_3], [CO_2] and [*O*] are respectively the densities of hydrogen, ozone, carbon dioxide and oxygen. K^O is the rate coefficient of reaction (5) (*García Muñoz et al.,* 2005). Each density profile will be presented in section 3.1. The quenching coefficients by CO_2 ($k_T^{CO_2}$, k^{CO_2}) and oxygen (k^O) will be discussed in section 3.2 and the various quenching processes by CO_2 will be detailed in section 3.3.

1.4. Density profiles

Density profiles of several constituents must be adopted to model the OH nightglow vertical distribution. In order to root as much as possible the model calculations into recent measurements, we have adopted density values derived from recent studies of airglow emissions and stellar occultations made on board Venus Express.

The ozone density profile (Figure 3, solid line) is based on observations by *Montmessin et al.* (2011) who detected ozone in the Venus thermosphere for the first time. They used the

SPectroscopy for Investigation of Characteristics of the Atmosphere of Venus (SPICAV) instrument on board Venus Express in a stellar occultation observation mode (*Bertaux et al.*, 2007). During an occultation, the spectrum of a selected hot star is first recorded above the atmosphere where it is unaltered by atmospheric absorption and can be used as a reference spectrum. As the spacecraft moves towards its pericenter, the star spectrum is progressively occulted by the atmosphere and may be compared to the reference. This technique leads to an absolute concentration of O_3 derived from a relative measurement (independent of the absolute instrument calibration) with a less than 1 km spatial resolution (*Bertaux et al.*, 2007). Using 29 stellar occultation detections of ozone, *Montmessin et al.* (2011) deduced that the O_3 layer is on the average located at 99±10 km with a peak value ranging from 10^7 to 10^8 molecules cm^{-3}. However, densities at only 1 to 3 altitudes around the peak are measured by SPICAV with sufficient signal to noise ratio. To obtain a smooth continuous profile, we adopt the O_3 density profile calculated with *Krasnopolsky* (2010)'s model, which peaks at 93.5 km, but normalized it to the mean observed peak of 6.0×10^7 cm^{-3}. This one-dimensional photochemical model involves 61 reactions and 24 species and was specifically adapted to the Venus nightside. As discussed by *Montmessin et al.* (2011), the observed ozone peak density is significantly less than the modelled 3.9×10^9 cm^{-3}, probably because the chlorine mixing ratio was underestimated in the photochemical model. Also, one-dimensional models do not consider the global circulation of the atmosphere, which is however very important to correctly reproduce density distributions (*Brecht et al.*, 2011, 2012). Taking a profile resulting from a 3-D model would be highly valuable to this study but, unfortunately, no such profile is available at the moment. The role of the ozone peak altitude on the OH airglow distribution will be discussed in section 3.4.

Since no observed atomic hydrogen profile is available, the shape of this profile has to be taken from photochemical models as well. They all show a relatively flat distribution between

95 and 115 km. *Krasnopolsky* (2010)'s model calculates a peak density of 7.5×10^6 cm^{-3}, a value compatible with his large ozone density profile but much too small to match both the SPICAV observations of the O_3 density and the OH observed intensities presented in section 2.3. We thus decided to adopt the value predicted by *Krasnopolsky and Parshev* (1981), *Yung and Demore* (1982) and *Pernice et al.* (2004) of $\sim 1 \times 10^8$ cm^{-3}. The H adopted density profile is shown in Figure 3. Once again, if available, using a hydrogen density profile resulting from a 3-dimensional model would be more realistic than a one-dimensional approach.

The adopted CO_2 density profile (Figure 3, solid line) is derived from the analysis by *Soret et al.* (2012) of 114 observed CO_2 density profiles extracted by *Montmessin et al.* (2006) from SPICAV stellar occultations. On the basis of the location of these individual profiles on the nightside and their distances to the antisolar point, *Soret et al.* (2012) generated a three-dimensional statistical map of the CO_2 density. The profile, shown in Figure 3, is the mean CO_2 density profile averaged over the Venus nightside. It is more appropriate, although not drastically different, to use this profile rather than a CO_2 profile from the VTS3 empirical model (dashed line). The VTS3 densities below 145 km are extrapolations based on hydrostatic equilibrium of higher altitude measurements by the Pioneer Venus orbiter (*Hedin et al.*, 1983).

The oxygen density vertical distribution plotted in Figure 3 is the averaged profile of the three-dimensional statistical map obtained by *Soret et al.* (2012). To build up this map, they used VIRTIS limb and nadir observations of the $O_2(a^1\Delta)$ nightglow at 1.27 μm, from which they derived the O density from the relationship between the oxygen three-body recombination rate and the $O_2(a^1\Delta)$ intensity. The density of CO_2, acting as the third body, was based on the SPICAV stellar occultations, as described before, and is thus fully consistent with the value adopted in this study. The averaged O density profile presented in Figure 3 peaks at 103.5 km with a maximum value of 1.9×10^{11} cm^{-3}. This value compares very well

with the oxygen density profile calculated by *Brecht et al.* (2012). Their three-dimensional Venus Thermospheric General Circulation Model (VTGCM, *Bougher et al.*, 1990), which combines chemical, dynamical and energetic processes, calculates an average nightside oxygen peak density of 1.4×10^{11} cm^{-3} at 104 km.

1.5. Quenching coefficients

To simulate the OH collisional deactivation by O and CO_2 (reactions 4 and 6), it is necessary to determine the value of the quenching coefficients. So far, only the $k^O\left(v'=0,1,2,3,4,7,9\right)$ oxygen quenching coefficients have been measured (*Thiebaud et al.*, 2010; *Kalogerakis et al.*, 2011). The missing values of $k^O\left(v'=5,6,8\right)$ have been interpolated. The CO_2 quenching coefficients $k_T^{CO_2}$ have been measured up to v'=12 except for v'=5 and v'=6. These values have been interpolated with a $\log_{10}\left(k_T^{CO_2}\right)-v'$ law (*García Muñoz et al.,* 2005). These measurements were made at room temperature, while the OH emission takes place in a region where the temperature is ~185 K. *Romanescu et al.* (2009) and *Thiebaud et al.* (2010) demonstrated that both the O and CO_2 quenching coefficients are highly dependent on temperature. *Thiebaud et al.* (2010) deduced from their experiments that a linear law could fit the dependence of $k^O\left(v'=7\right)$ with temperatures between 160 and 300 K, the quenching coefficient being slower at lower temperature. In this study, we scale down all their oxygen quenching coefficients by a factor of 0.77, which corresponds to the $k^O_{185K}\left(v'=7\right)/k^O_{296K}\left(v'=7\right)$ ratio. The O quenching coefficients calculated at 185 K are given in Table 1. These values must be multiplied by 0.95 or 1.04 to obtain the oxygen quenching coefficients at 170 K or 200 K, respectively.

For the CO_2 quenching coefficients, *Romanescu et al.* (2009) found that for v'=1 to v'=3, $k_T^{CO_2}(v',185K)/k_T^{CO_2}(v',300K)=1.6$. At ambient temperature these vibrational quenching coefficients are 1.42 time larger than the value adopted by *García Muñoz et al.* (2005). We thus normalize the *García Muñoz et al.*'s values at 300 K and extrapolate the data by *Romanescu et al.* (2009) at 300 K for any vibrational level up to v'=9. Table 1 summarizes for each vibrational level the direct fractional yield and the adopted quenching coefficients of OH(v) by O and CO_2 at 185 K. A lower temperature of 170 K has a negligible impact on the CO_2 quenching coefficients. At 200 K, the ratio $k_T^{CO_2}(v',170K)/k_T^{CO_2}(v',300K)=2.0$ should be used.

1.6. Sudden Death and Single Quantum schemes

All quantities mentioned in equation (8) have been described in the previous sections with the exception of k^{CO_2}. Its value depends on the mode of the vibrational collisional of excited OH by CO_2. In the "Sudden Death" model, the vibrationally excited OH molecule is completely deactivated following a collision with the quenching molecule (Figure 4a). This mechanism can be expressed by:

$$\begin{cases} k^{co_2}(v',v''=0)=k_T^{CO_2}(v') \\ k^{co_2}(v',v''\neq 0)=0 \end{cases} \quad \textbf{(9)}$$

The second model considered in this study is the "Single Quantum" model where the excited OH molecule relaxes one single quantum level at a time (Figure 4b). The Single Quantum model can be expressed by:

$$\begin{cases} k^{co_2}\left(v', v'' = v'-1\right) = k_T^{CO_2}\left(v'\right) \\ k^{co_2}\left(v', v'' \neq v'-1\right) = 0 \end{cases} \quad \textbf{(10)}$$

Model results exposed in section 3.4 will compare the output of both models with those of the observational statistical study presented in section 2.

1.7. Model results

VIRTIS limb observations show that (i) both OH spectral sequences peak near 97 km, (ii) the Δv=1 emission layer is located ~0.8 km higher than Δv=2 and (iii) I_2/I_1=0.38±0.37. Using synthetic spectra to analyse the average limb spectrum, we have found that the Δv=1 sequence is composed of the (1-0), (2-1), (3-2) and (4-3) bands. To clarify why only low vibrational levels populate these emissions, while the Bates-Nicolet mechanism predicts the population of higher vibrational levels, we use numerical simulations with the non-LTE model described in section 3.3. As previously mentioned, we adopt O_3, CO_2 and O density profiles rooted in recent studies based on Venus Express measurements. We use CO_2 and O temperature dependent quenching coefficients derived from recent laboratory results extrapolated at 185 K, which is the temperature of the airglow layer. Two different approaches for quenching by CO_2 have been considered.

Using equation 8, it is possible to calculate the relative contribution of each transition to the total brightness of the sequence. With the Sudden Death model, the (1-0), (2-1), (3-2) and (4-3) bands represent 7.6%, 12.1%, 4.0% and 41.3% of I_1, respectively. These relative contributions are very different from those found in section 2.2 for two main reasons. First, the total of those contributions do not reach 100% for both sequences. This is because the Sudden Death model does not correctly predict the observed spectral distribution. For

example, the (4-3) transition is not observed to significantly contribute. Similarly, the (9-8) modelled transition would be a significant fraction of the Δv=1 sequence which, given the results of the synthetic spectrum, is clearly unrealistic. To make it more obvious, the spectrum of Δv=1, generated using the Sudden Death steady-state vibrational populations, is shown in Figure 5c (in red) and compared with the observations (in black). It appears that the main contribution between 2.7 and 3.1 μm is clearly underestimated.

Considering now the Single Quantum model, the relative contributions of the (1-0), (2-1), (3-2) and (4-3) transitions are found to be 54.8%, 30.5%, 10.4% and 3.8% of the Δv=1 sequence. These relative contributions are in fair agreement with those obtained with the synthetic spectrum and 99.5% of the Δv=1 sequence is well reproduced by the Single Quantum model. Figure 5d confirms that the Single Quantum model satisfactorily reproduces the Δv=1 spectrum as the synthetic spectrum shown in red was generated using the Single Quantum ratios. By contrast, the Δv=2 structure is not well modelled as only 50.4% of I_2 is reproduced by the synthetic model. This result has to be taken with care since this segment of the VIRTIS spectrum is very noisy and the Δv=2 emission may be too weak to be properly detected and accurately corrected from additional contributions. These discrepancies clearly demonstrate that the Sudden Death model cannot, by far, reproduce the characteristics of the OH Meinel bands observed in the Venus upper mesosphere.

It is also possible to compare the model predictions to the limb observations presented in section 2.3. We previously described how we calculate the OH* density profile for a given vibrational level. The associated limb intensity profile is obtained by applying the Abel transform (which integrates the volume emission rate along the line of sight) to the product of the O_3 and H density profiles by the spontaneous transition probability coefficient. At a given altitude z_0, the total intensities I_1 and I_2 of the Δv=1 and Δv=2 sequences are given by the following equations:

$$I_1(z_0) = \sum_{v^*=1}^{9} \left[\int_{z_0}^{+\infty} 2 \times \frac{z}{\sqrt{z^2 - z_0^2}} \times A(v' = v^*, v'' = v^* - 1) \times \left[OH(v' = v^*) \right](z_0)\, dz \right] \quad \textbf{(11)}$$

$$I_2(z_0) = \sum_{v^*=2}^{9} \left[\int_{z_0}^{+\infty} 2 \times \frac{z}{\sqrt{z^2 - z_0^2}} \times A(v' = v^*, v'' = v^* - 2) \times \left[OH(v' = v^*) \right](z_0)\, dz \right] \quad \textbf{(12)}$$

The corresponding Δv=1 and Δv=2 limb intensities are represented in Figure 5a for the Sudden Death model and Figure 5b for the Single Quantum model.

For the Sudden Death model, the Δv=1 limb intensity peaks at 94.5 km with a value of 9.74 kR while the Δv=2 intensity reaches 53.4 kR at 94.0 km. The larger value of the Δv=2 intensity compared to Δv=1 is a consequence of the direct population rate which favors vibrational levels v' = 6 to 9, whose radiative transitions significantly contribute to the Δv=2 sequence. The difference of altitude d=0.5 km is comparable to the value of 0.8 found in the statistical study section, but both altitudes are too low (~94 km) in comparison with the observations (~97 km). The absolute limb intensities are too low as well by a factor of 36 and 2.4 for the Δv=1 and Δv=2 limb intensities, respectively. Also, the calculated Δv=2 emission is about 5.5 times brighter than the Δv=1 calculated intensity, which is far from the measured range of values of I_2/I_1=0.38±0.37. These discrepancies, together with the incorrect spectral composition definitely rule out the Sudden Death model as a possible candidate to reproduce the OH Venus nightglow observations.

In the Single Quantum model, both the Δv=1 and Δv=2 emissions peak at 94.0 km with values of 2.05 MR and 1.04 MR, respectively. These intensities are about 6 times higher than the observed values but the ratio I_2/I_1=0.51 is in a much better agreement with the value of 0.38±0.37 found in the statistical study. For this reason, in the following discussion, we concentrate on the Δv=1 sequence.

4. Model sensitivity tests

We now examine the sensitivity of our results by modifying the input density profiles and the values of the quenching coefficients.

1.8. Density profiles sensitivity tests

As discussed in section 3.1, the O density profile was taken from *Soret et al.* (2012)'s analysis of the $O_2(a^1\Delta)$ night airglow. A different density O profile could be used, such as that from *Krasnopolsky* (2010)'s one-dimensional model, which peaks at 110 km with a maximum value of $2.0x10^{11}$ cm^{-3}, but simulations indicate that it would not affect the results. Actually, a null oxygen density profile only slightly increases the I_1 Single Quantum intensity. Consequently, reaction (5) and OH* quenching by O atoms only play a minor role.

By contrast, if the CO_2 density profile from the VTS3 empirical model calculated for midnight LT at the equator is adopted (Figure 3, dashed line), the intensity values decrease and the peak altitudes increase. For the Single Quantum model, I_1=0.78 MR at 95.5 km and I_2=0.40 MR at 95.5 km.

If we use the O and CO_2 profiles from *Soret et al.* (2012) but shift the O_3 density profile upward by 5.5 km (so that its maximum reaches the mean altitude of 99 km observed by *Montmessin et al.*, 2011), both Δv sequences peak at ~99 km, compared to 94 km when the ozone maximum is located at 93.5 km. Therefore, as expected, the characteristics of the ozone layer mainly control the altitude of the OH emission, a consequence of the rather flat H density profile in this region. The value of the ozone density peak also critically influences the calculated OH intensities. For example, considering an O_3 density profile peaking at $9.3x10^6$

cm^{-3} at 93.5 km with the Single Quantum model, the calculated OH profiles peak too low but their intensities are in good agreement with the observed values of I_1=0.35 MR and I_2=0.13. This ozone density value is in the lower range of the detections reported by *Montmessin et al.* (2011), but consistent with the fact that ozone was unambiguously detected in only 10 % of the nightside stellar occultations. It is indeed likely that the O_3 density in the upper mesosphere is generally below the SPICAV detection threshold of ~$9.3x10^6$ cm^{-3}.

If we adopt all the density profiles (O_3, CO_2, O and H) from *Krasnopolsky* (2010), the intensities calculated with the Single Quantum model would be I_1=4.40 MR and I_2=2.26 MR. Despite a much lower H density than that used in this study which partly compensates for the larger amount of ozone density, the retrieved OH intensities would be much too high in comparison with the observations.

1.9. Quenching coefficients sensitivity tests

While density profiles can clearly influence the global morphology of the OH limb profiles, quenching processes also control the shape and the total intensity of the OH spectra. The impact of uncertainties on quenching coefficient has also been tested. If the original quenching coefficients from *García Muñoz et al.* (2005) are considered and the density profiles are those described in section 3.1, the contribution for of (1-0), (2-1), (3-2), (4-3), (2-0) and (3-1) bands are 13.3%, 19.5%, 8.6%, 35.2%, 1.6% and 2.2% respectively for the Sudden Death model and 52.9%, 30.9%, 11.1%, 4.2%, 23.0% and 25.2% for the Single Quantum model. Even though these relative contributions are slightly different from those found in section 2.2, they do not strongly affect the global shape of the spectra and the Sudden Death model once again does not correctly reproduce the VIRTIS observed spectrum.

Considering the exact same density profiles and the values of the O and CO_2 quenching coefficients at 170 K determined in section 3.2, no difference is predicted by the model. This can easily be explained since quenching by O atoms is negligible (section 4.1) and $k_T^{CO_2}(v',170K) = k_T^{CO_2}(v',185K)$. If a temperature of 200 K is adopted, the relative contribution of each band is modified by less than 1 % and the intensities slightly decrease. In this case, I_1=1.68 MR and I_2=0.85 MR at 94.0 km for the Single Quantum model. At 200 K, the best agreement with the observed VIRTIS results is obtained with an O_3 density profile peaking at 96.5 km at a value of 7.0×10^6 cm^{-3}. Therefore, no matter the uncertainties in the quenching coefficients values, the Single Quantum model satisfactorily reproduces the Δv=1 observations.

1.10. Best fit case

This sensitivity study showed that some parameters are more influent same some others. However, some of them have been characterized more precisely than others. For instance, it seems more appropriate to use density profiles from recent measurements than those derived from one-dimensional models. Thus, the CO_2 and O density profiles by *Soret et al.* (2012) described in section 3.1 have been used as input parameters of our best fit case (Figure 3, solid lines). Likewise, it seems more realistic to take into account the dependence on temperature of the quenching coefficients. Those used for the best fit case are shown in Table 1 at 185 K. Since no measurement of the hydrogen density has been made, we decided to use that described in section 3.1 and shown in Figure 3 (solid line). Sections 3 and 4 demonstrated that the Single Quantum model reproduces the OH observations much more correctly than the Sudden Death model. The Single Quantum model is thus used for the best match. Finally, the O_3 density profile has to match the recent SPICAV observations. Because of the small

number of positive detections and the limited vertical resolution of the measurements, the only constraints on the O_3 profile are: (i) a peak density at 99±10 km; (ii) a peak value ranging from 10^7 to 10^8 molecules cm^{-3} for the brightest detctions.

To model I_1=0.35 MR and I_2=0.13 MR peak intensity values near 97 km and a ratio I_2/I_1=0.38±0.37 corresponding to the VIRTIS observations, the input ozone density profile has to peak at $5.8x10^6$ cm^{-3} at 96.5 km (Figure 3, dashed line). In this case, the calculated Δv=1 intensity reaches 0.33 MR at 96.5 km and the Δv=2 intensity is 0.17 MR at 96.5 km, in good agreement with the observations, considering the uncertainties on the Δv=2 values.

.

1.11. Discussion

Even if our results suggest that the Single Quantum mechanism provide a better description of the OH(v) quenching by CO_2 over the Sudden Death model, a third approach, the Cascade model which considers any transition to a lower vibrational level as possible, may also be relevant to the Venus atmosphere. It was not considered here because transition probabilities are unknown and no experimental or theoretical basis currently exists to build such a model. In their analysis of the terrestrial OH limb spectra observed with the SCIAMACHY spectrometer, *Kaufmann et al.* (2008) also concluded that a mixture of multi quantum and single quantum relaxation models provides the best agreement with the observed visible spectra, even though no quantitative data have been published.

We also note that the PGOPHER synthetic spectrum of the Δv=1 sequence underestimates some spectral lines. The (1-0) band structure is very well reproduced at 2.75 µm and 2.81 µm. Similarly, the main (2-1) and (3-2) peaks respectively located at 2.95 and 3.10 µm, are

correctly predicted. Instead, the (1-0), (2-1) and (3-2) secondary peaks at 2.91, 3.06 and 3.21 μm are always underestimated. These differences may be related to the fact that the VIRTIS spectrum is averaged over different observing conditions. Another possibility is that some of the line intensity parameters used in the calculation of the synthetic spectrum have not been measured with a sufficient accuracy. Finally, a possibility exists that some additional unidentified spectral features are produced by another unidentified constituent.

5. Conclusions

Limb spectra of the Venus nightglow emission of OH Meinel bands collected with the VIRTIS infrared imaging spectrograph on board Venus Express during 2.5 years have been analyzed. Our statistical analysis indicates that the intensity and altitude of the $\Delta v=1$ and $\Delta v=2$ sequences are not anti-correlated. Statistically, the altitude of the maximum of the $\Delta v=2$ emission is located approximately 0.8 km lower than $\Delta v=1$. Although the O_3 + H Bates-Nicolet reaction produces most of the excited OH molecules in vibrational levels v'=6 to 9, only bands originating from v' = 1 to 4 are detected in the VIRTIS spectra.

A steady-state model of the vibrational population considering direct population by O_3 + H reaction, radiative transitions and collisional quenching has been used to compare the expected spectral distribution, the altitude of the emission peak and the emission rate with the observations. The neutral densities used in the model are rooted in recent Venus Express remote sensing measurements. The CO_2 density profile was derived from stellar occultations with the SPICAV instrument. Similarly, the ozone peak density is based on the recent SPICAV detections of an ozone layer near 110 km by *Montmessin et al.* (2011). The O vertical distribution is obtained from the analysis of the $O_2(a^1\Delta)$ emission at 1.27 μm observed with the VIRTIS instrument. Only the H density profile is not presently constrained by

observational data. Its shape and peak density have been taken from photochemical model predictions.

We find that the "Sudden Death" quenching scheme by CO_2 provides inadequate intensity distribution between the various bands and insufficient airglow brightness within a reasonable range of parameters such as the neutral density profiles and quenching coefficients. Instead, the distribution of the $\Delta v=1$ spectrum modeled with the single quantum quenching scheme by CO_2 is in good agreement with the VIRTIS observations, despite some minor differences. We suggest that a combination of an essentially single quantum jump relaxation with a moderate multi quantum cascade component provides the best agreement with the VIRTIS spectra.

Once the quenching scheme is adopted, the brightness of the OH nightglow essentially constrains the product of the O_3 and H densities. Photochemical models predict a flat H density distribution in the mesosphere-thermosphere transition region, although some disagreement exists on the absolute H density. Therefore, the altitude of the ozone layer essentially controls that of the OH emission and the O_3 density peak is expected to be located in the vicinity of 97 km, the mean altitude of the maximum OH emission. This conclusion is in full agreement with the SPICAV observations where the ozone layer was detected between 90 and 120 km, with a mean value of 99 km. Although not unique, we find that a combination of an ozone peak close to 10^7 cm^{-3} at 96.5 km, corresponding to the faintest SPICAV detections, together with a hydrogen density of $\sim 1x10^8$ cm^{-3} provides excellent agreement with the VIRTIS OH nightglow observations. This study is in agreement with the conclusion by *Montmessin et al.* (2011) who suggested that the O_3 density values from the one-dimensional model of *Krasnopolsky* (2010) are about 2 orders of magnitude too high. They indicated that this is a likely consequence of a too low concentration of chlorine, which limits the destruction of ozone and leads to an overestimate of the O_3 density. Krasnopolsky

reproduced the first detection of hydroxyl emission in the Venus atmosphere by Piccioni et al. (2008). These observations were very bright (880 kR for the $\Delta v=1$ sequence and 100 kR for the $\Delta v=2$ sequence) compared to the statistical intensities reported in this study (350 kR and 130 kR, respectively). Krasnopolsky also assumed that only low OH vibrational levels ($v\leq2$) had to be populated while, in this study, we clearly show that the (3-2) band is part of the $\Delta v=1$ sequence. Finally, one-dimensional photochemical models can hardly predict nightside density profiles required for airglow production since these are dependent on the global circulation of the atmosphere (*Brecht et al.*, 2011; 2012). For this matter, it would be highly valuable to base future studies on ozone and hydrogen density profiles calculated with three-dimensional models coupling global circulation and photochemistry.

Acknowledgements

We gratefully thank all members of the ESA Venus Express project and of the VIRTIS and SPICAV scientific and technical teams. We also thank V. Krasnopolsky for providing model values, C. Western whose help with the PGOPHER software has been most valuable, K. Kalogerakis for useful discussions and P. Gérard for his valuable contribution to the statistical tests. L. Soret was supported by the PRODEX program managed by the European Space Agency with the help of the Belgian Federal Space Science Policy Office. J.-C. Gérard acknowledges funding from the Belgian Fund for Scientific Research (FNRS). This work was also funded by Agenzia Spaziale Italiana and the Centre National d'Etudes Spatiales.

References

Bailey, J., V. S. Meadows, S. Chamberlain, and D. Crisp (2008), The temperature of the Venus mesosphere from O_2 ($a^1\Delta_g$) airglow observations, Icarus, 197, 247-259.

Bates, D. R., and M. Nicolet (1950), Atmospheric Hydrogen, Publications of the Astronomical Society of the Pacific 62, 106.

Bernath, P. F. and R. Colin (2009), Revised molecular constants and term values for the $X^2\Pi$ and $B^2\Sigma^+$ states of OH, Journal of Molecular Spectroscopy, 257, 20–23.

Bertaux, J.-L., et al. (2007), SPICAV on Venus Express: Three spectrometers to study the global structure and composition of the Venus atmosphere, Planet. Space Sci., 55, 1673-1700.

Bougher, S. W., J. C. Gérard, A. I. F. Stewart, and C. G. Fesen (1990), The Venus Nitric Oxide Night Airglow: Model Calculations Based on the Venus Thermospheric General Circulation Model, J. Geophys. Res., 95, 6271-6284.

Brecht, A. S., S. W. Bougher, J.-C. Gerard, C. Parkinson, S. Rafkin, and B. Foster (2011), Understanding the Variability of Nightside Temperatures, NO UV and O_2 IR Nightglow Emissions in the Venus Upper Atmosphere, J. Geophys. Res., 116, E08004.

Brecht, A. S., S. W. Bougher, J. C. Gérard, and L. Soret (2012), Atomic oxygen distributions in the Venus thermosphere: Comparisons between Venus Express observations and global model simulations, Icarus, 217, 2, 759-766.

Drossart, P., et al. (2007), Scientific goals for the observation of Venus by VIRTIS on ESA/Venus express mission, Planet. Space Sci., 55, 1653-1672.

García Muñoz, A., J. C. McConnell, I. C. McDade, and S. M. L. Melo (2005), Airglow on Mars: Some model expectations for the OH Meinel bands and the O_2 IR atmospheric band, Icarus, 176, 75-95.

Gérard, J. C., L. Soret, A. Saglam, G. Piccioni, and P. Drossart (2010), The distributions of the OH Meinel and $O_2(a^1\Delta\text{-}X^3\sum)$ nightglow emissions in the Venus mesosphere based on VIRTIS observations, Adv. Space Res., 45, 1268-1275.

Hedin, A. E., H. B. Niemann, W. T. Kasprzak, and A. Seiff (1983), Global Empirical Model of The Venus Thermosphere, J. Geophys. Res., 88(A1), 73-83.

Kalogerakis, K., G. P. Smith and R. A. Copeland (2011), Collisional removal of OH($X^2\Pi$, v = 9) by O, O_2, O_3, N_2, and CO_2, J. Geophys. Res., 116, D20307.

Kaufmann, M., C. Lehmann, L. Hoffmann, B. Funke, M. López-Puertas, C. V. Savigny, and M. Riese (2008), Chemical heating rates derived from SCIAMACHY vibrationally excited OH limb emission spectra, Adv. Space Res., 41, 1914-1920.

Krasnopolsky, V. A., and V. A. Parshev (1981), Chemical composition of the atmosphere of Venus, Nature, 292, 610-613.

Krasnopolsky, V. A. (2010), Venus night airglow: Ground-based detection of OH, observations of O_2 emissions, and photochemical model, Icarus, 207(1), 17-27.

Krasnopolsky, V. A. (2011), Atmospheric chemistry on Venus, Earth, and Mars: Main features and comparison, Planet. Space Sci., 59(10), 952-964.

Meinel, A. B. (1950), OH emission bands in the spectrum of the night sky, Astrophys. J., 111(555).

Meriwether, J. W. (1989), A Review of the photochemistry of selected nightglow emissions from the mesopause, J. Geophys. Res., 94, 14629-14646.

Migliorini, A., G. Piccioni, A. Cardesín Moinelo, and P. Drossart (2010), Hydroxyl airglow on Venus in comparison with Earth, Planet. Space Sci., 59, 974-980.

Montmessin, F., E. Quémerais, J. L. Bertaux, O. Korablev, P. Rannou, and S. Lebonnois (2006), Stellar occultations at UV wavelengths by the SPICAM instrument: Retrieval and analysis of Martian haze profiles, J. Geophys. Res., 11, E09S09.

Montmessin, F., J. L. Bertaux, F. Lefèvre, E. Marcq, D. Belyaev, J. C. Gérard, O. Korablev, A. Fedorova, V. Sarago, and A.-C. Vandaele (2011), A layer of ozone detected in the upper atmosphere of Venus nightside, Icarus, 216, 1, 82-85.

Murphy, R. E. (1971), Infrared Emission of OH in the Fundamental and First Overtone Bands, J. Chem. Phys., 54, 4852-4859.

Ohoyama, H., T. Kasai, Y. Yoshimura, H. Kimura, and K. Kuwata (1985), Initial distribution of vibration of the OH radicals produced in the H + O_3 → OH($X^2\Pi$1/2,3/2) + O_2 reaction. Chemiluminescence by a crossed beam technique, Chemical Physics Letters, 118, 263-266.

Ohtsuki, S., N. Iwagami, H. Sagawa, M. Ueno, Y. Kasaba, T. Imamura, K. Yanagisawa and E. Nishihara (2008), Distributions of the Venus 1.27-mm O_2 airglow and rotational temperature, Planet. Space Sci, 56, 1391–1398.

Pernice, H., P. Garcia, H. Willner, J. S. Francisco, F. P. Mills, M. Allen, and Y. L. Yung (2004), Laboratory evidence for a key intermediate in the Venus atmosphere: Peroxychloroformyl radical, P. Natl Acad Sci USA, 101, 14007-14010.

Piccioni, G., et al. (2008), First detection of hydroxyl in the atmosphere of Venus, Astronomy & Astrophysics, 483, L29-L33.

Piccioni, G., L. Zasova, A. Migliorini, P. Drossart, A. Shakun, A. G. Munoz, F. P. Mills, and A. Cardesin-Moinelo (2009), Near-IR oxygen nightglow observed by VIRTIS in the Venus upper atmosphere, J. Geophys. Res., 114, E00B38.

Romanescu, C., A. Marakov, H. Timmers, K. S. Kalogerakis, and R. A. Copeland (2009), Temperature Dependence of the Vibrational Relaxation of OH(v=1 and 2) by CO_2, abstract #P33A-1270, American Geophysical Union Fall meeting, San Francisco.

Sander, S. P., et al. (2003), Chemical Kinetics and Photochemical Data for Use in Atmospheric Studies, JPL publication, 02-25.

Soret, L., J.-C. Gérard, G. Piccioni, and P. Drossart (2010), Venus OH nightglow distribution based on VIRTIS limb observations from Venus Express, Geophys. Res. Lett., 37, L06805.

Soret, L., J. C. Gérard, F. Montmessin, G. Piccioni, P. Drossart, and J. L. Bertaux (2012), Atomic oxygen on the Venus nightside: Global distribution deduced from airglow mapping, Icarus, 217, 2, 849-855.

Thiebaud, J. E., R. A. Copeland, and K. S. Kalogerakis (2010), Vibrational Relaxation of OH(v=7) with O, O2 and H, abstract #SA43A-1752, American Geophysical Union Fall meeting, San Francisco.

Turnbull, D. N., and R. P. Lowe (1989), New hydroxyl transition probabilities and their importance in airglow studies, Planet. Space Sci., 37, 723-738.

Yung, Y. L., and W. B. Demore (1982), Photochemistry of the stratosphere of Venus: Implications for atmospheric evolution, Icarus, 51, 199-247.

Figure captions

Figure 1**:** The averaged spectra of the OH(Δv=1) (a) and the OH(Δv=2) (b) sequences from limb observations with VIRTIS-M are shown in black; the synthetic spectra are overplotted in red.

Figure 2**:** Histograms of the peak altitude (a) and of the peak intensity (b) observed with VIRTIS-M for the Δv=1 (in red) and Δv=2 (in black) emissions. For each limb profile, the Δv=2 peak altitude (c) and peak intensity (d) is plotted as a function of the Δv=1 peak altitude, and peak intensity. The bisector is plotted as a dashed line.

Figure 3**:** Density profiles used to model the OH Meinel emission. The hydrogen density profile is taken from *Krasnopolsky* (2010) normalized to a peak value of $1x10^8$ cm^{-3}. The averaged O and CO_2 density profiles are taken from *Soret et al.* (2012) (solid line). The dashed line is the CO_2 profile from VTS3 at 0° and 24:00 LT for low solar activity. A typical ozone density based on the SPICAV observations by *Montmessin et al.* (2011) combined with the altitude distribution calculated by *Krasnopolsky* (2010) is shown as a solid line. The O_3 density profile in dashed line corresponds to the best case of this study.

Figure 4**:** The two CO_2 quenching schemes considered in spectral simulations. The Sudden Death model (a) considers that the excited OH molecule will be totally deactivated after colliding with the quenching molecule while it will only relax by one single quantum level at a time in the Single Quantum model (b).

Figure 5**:** Limb profiles simulated with the Sudden Death model (left) and with the Single Quantum model (right). For each model, the OH (Δv=1) (in black) and OH (Δv=2) (in red) limb profiles are plotted in Figure 5a and Figure 5b, respectively. The VIRTIS spectrum of the Δv=1 sequence of Figure 1 is plotted in black in Figure 5c and Figure 5d to make comparison with the modeled spectra easier. The Sudden Death model (Figure 5c) cannot reproduce the observed spectrum while the Single Quantum model (Figure 5d) is in much better agreement.

Table 1: Fractional yields of OH vibrationally excited molecules used to model OH quenching by O atoms and CO_2 molecules (in $cm^3\ s^{-1}$).

v'	$f(v')$	$k^O(v',185K)$	$k_T^{CO_2}(v',185K)$
1	0.00	$3.08\text{x}10^{-11}$	$4.09\text{x}10^{-13}$
2	0.00	$3.77\text{x}10^{-11}$	$1.09\text{x}10^{-12}$
3	0.00	$6.16\text{x}10^{-11}$	$3.18\text{x}10^{-12}$
4	0.05	$8.47\text{x}10^{-11}$	$6.36\text{x}10^{-12}$
5	0.05	$1.46\text{x}10^{-10}$	$1.77\text{x}10^{-11}$
6	0.07	$2.31\text{x}10^{-10}$	$4.54\text{x}10^{-11}$
7	0.19	$2.70\text{x}10^{-10}$	$1.52\text{x}10^{-10}$
8	0.29	$3.00\text{x}10^{-10}$	$1.45\text{x}10^{-10}$
9	0.35	$3.08\text{x}10^{-10}$	$1.30\text{x}10^{-10}$

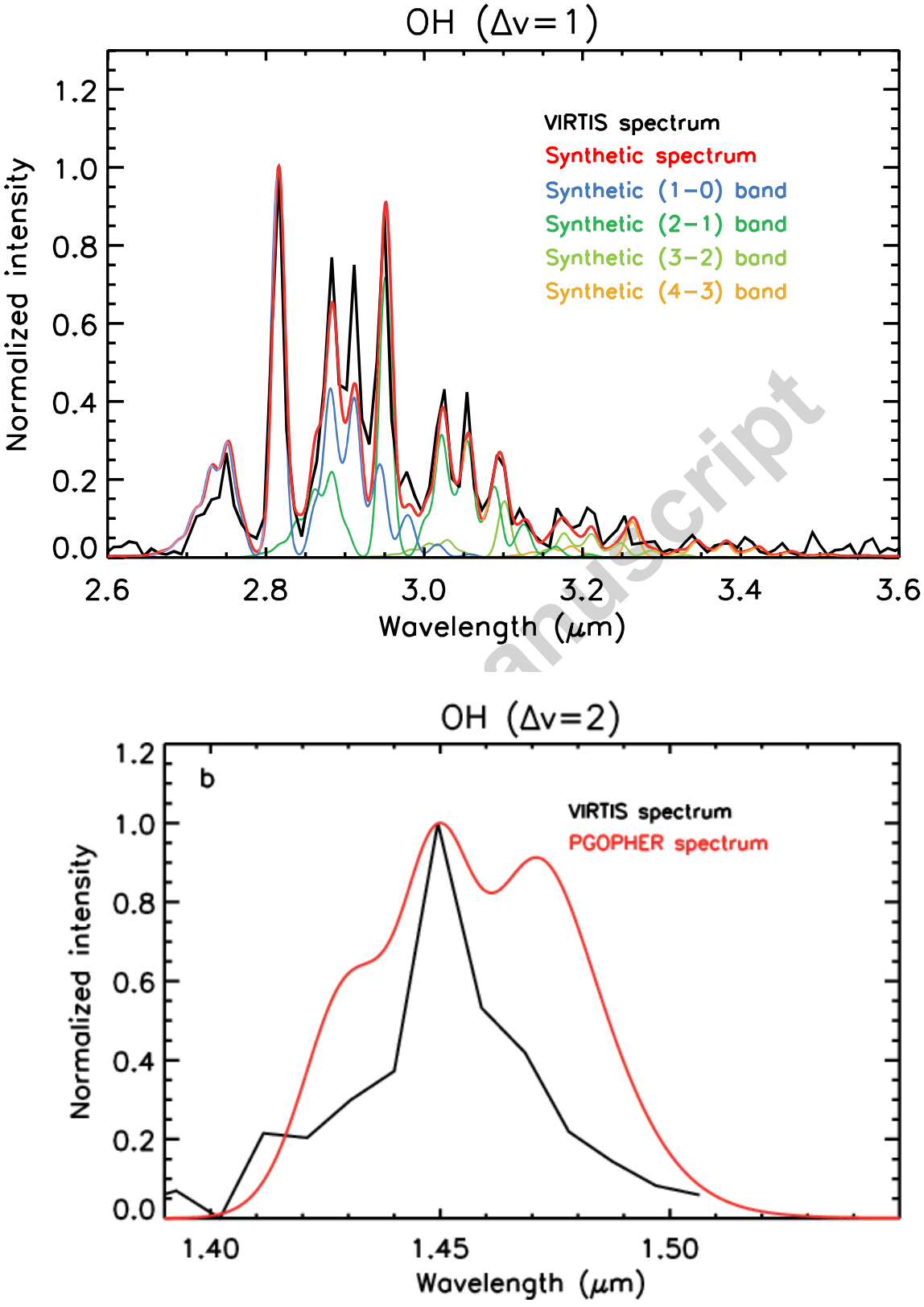

Figure 1 (a and b)

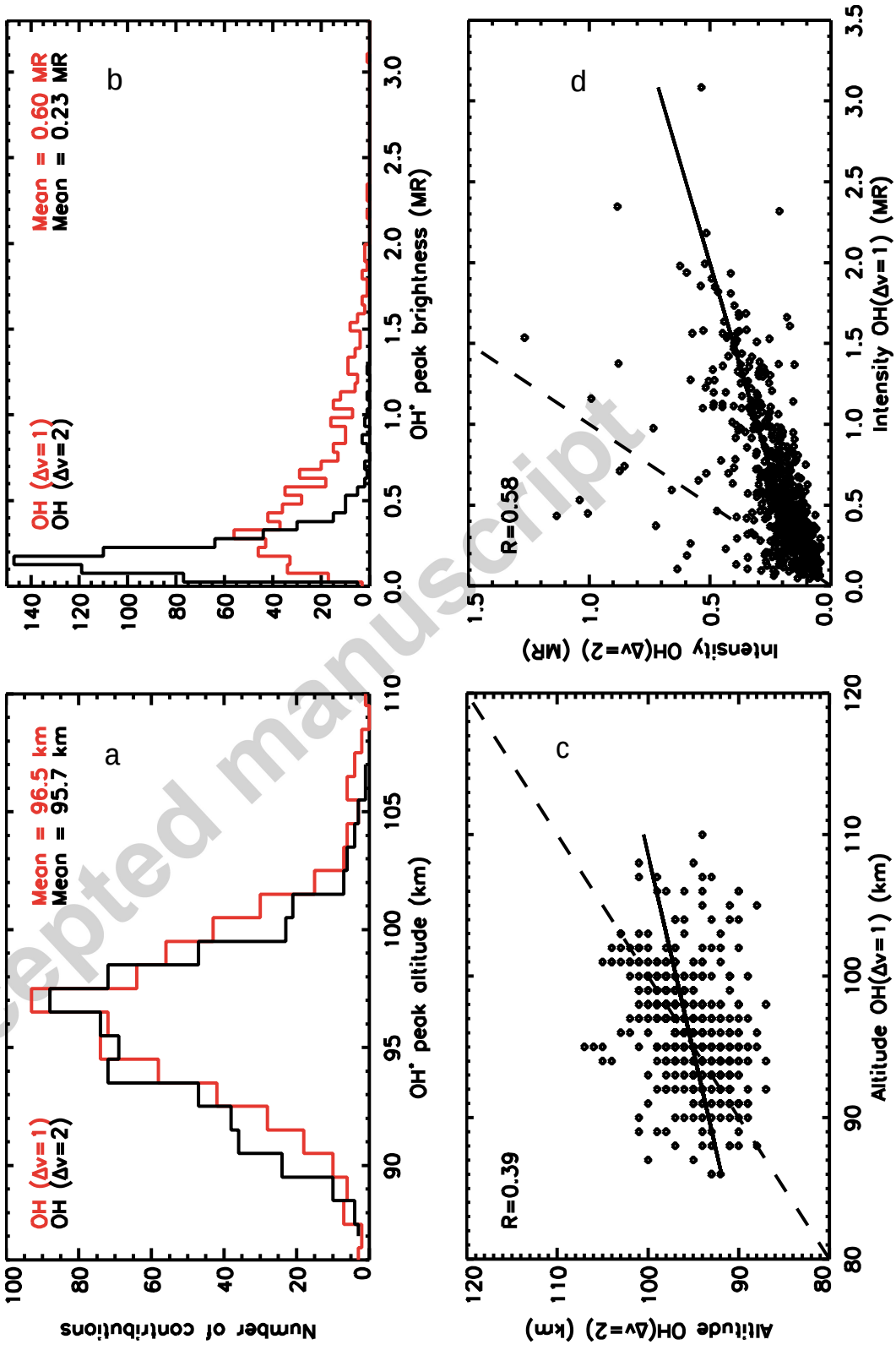

Figure 2 (a, b, c and d)

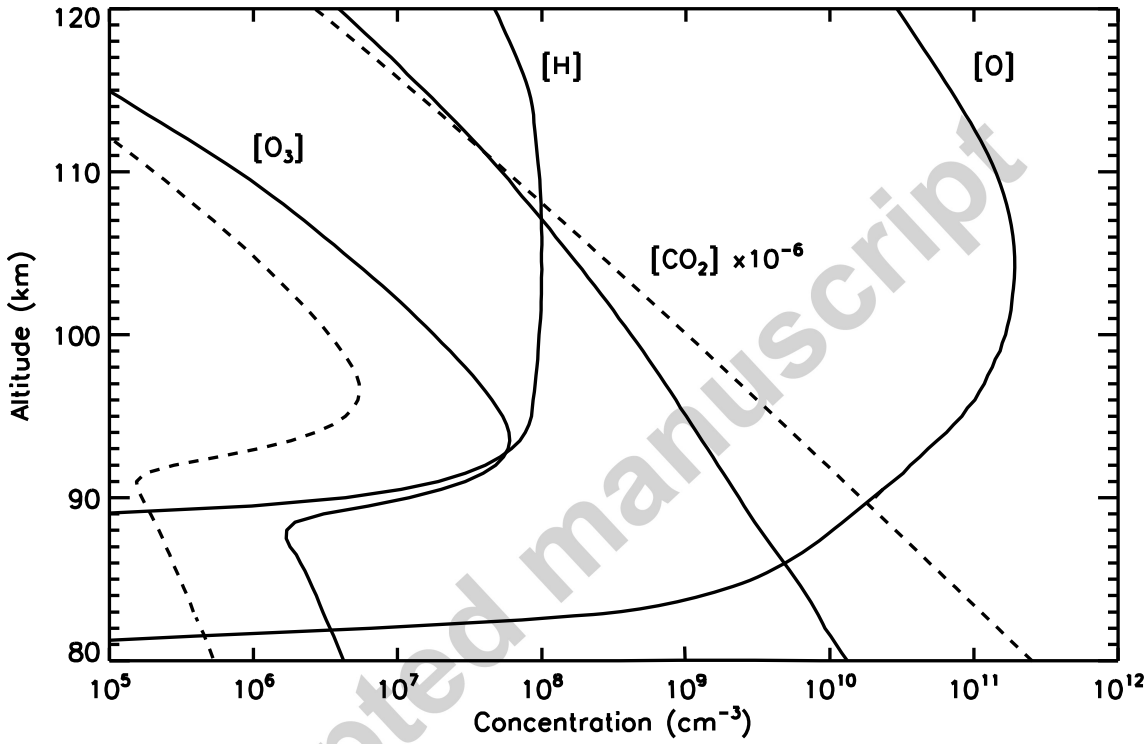

Figure 3

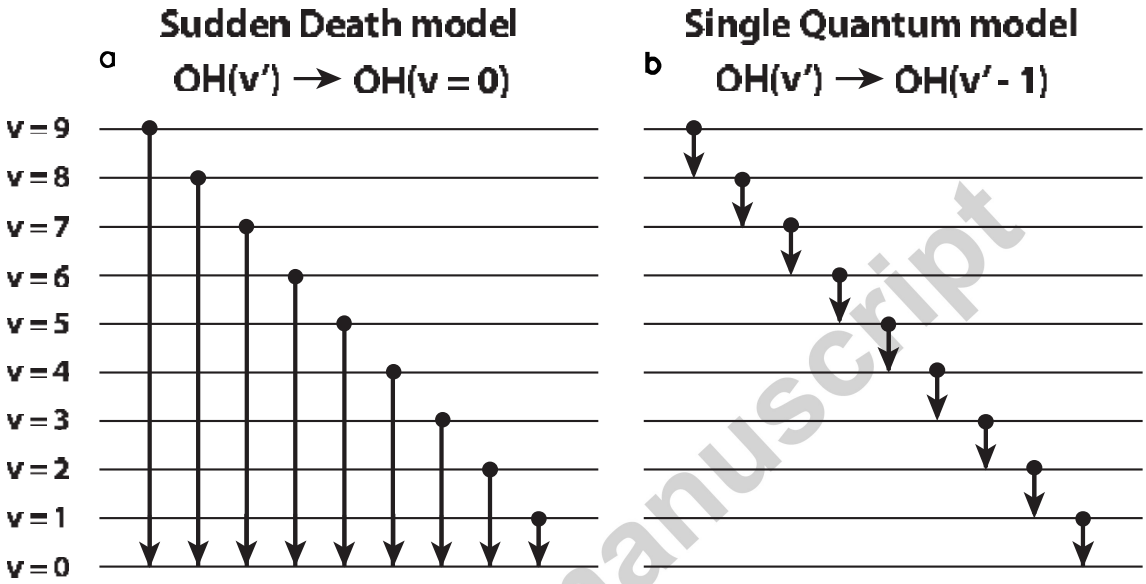

Figure 4 (a and b)

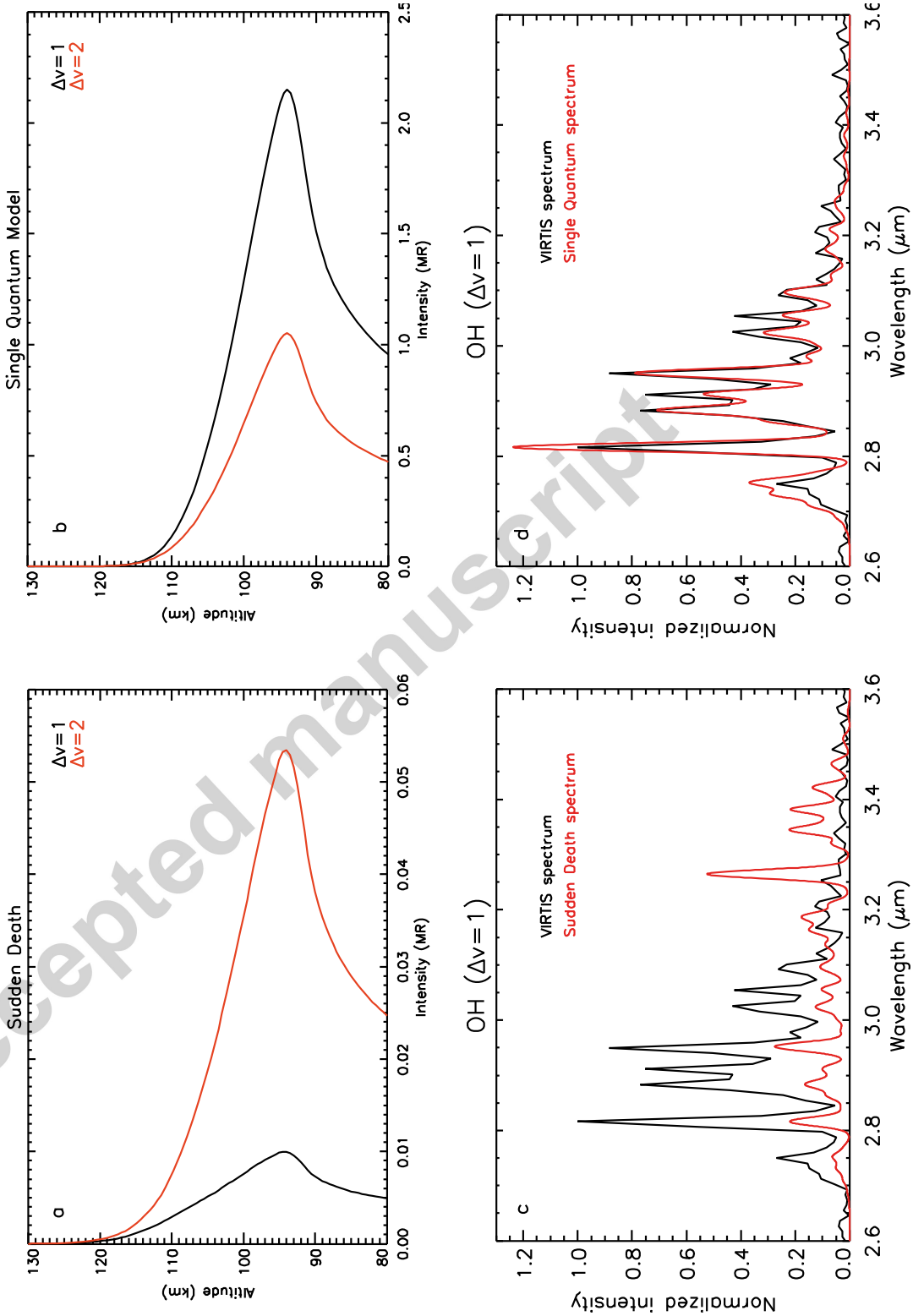

Figure 5 (a,b,c,d)